A Combined Wave Current Numerical Model: Part I, the wave model

George L. Mellor

Mark A. Donelan

July 2005

ABSTRACT

A surface wave model is developed which is to be coupled to three-dimensional ocean circulation models. It is based on a recent paper by Mellor (2003) wherein depth dependent coupling terms were derived. To be compatible with circulation models and to be numerically economical, this model is simplified somewhat compared to popular third generation models, but nevertheless does support depth and current refraction, other deep and shallow water effects and proper coupling with three-dimensional model derived currents.

1. Introduction

This paper follows papers by Mellor (2003, henceforth M03) and Mellor (2005, henceforth M05) which extended the phase averaged, wave-current equations of motion to the third vertical dimension. Previously, the wave interacting continuity and momentum equations were, a priori, vertically integrated (Phillips 1977) rendering them unsuitable for coupling with depth dependent numerical ocean circulation models. Now, as a consequence of M03, it is possible to couple three-dimensional circulation models with wave models; the coupling includes depth dependent wave radiation stress terms, Stokes drift, wave generated momentum transfer to the mean momentum equation, wave dissipation as a source term in the turbulence kinetic energy equation and mean current advection and refraction of wave energy.

The wave model described below, which parameterizes the frequency spectrum, increases the run time of a circulation model (the Princeton Ocean Model) by somewhat less than a factor of 2; the same horizontal grid is used for both models, a practical necessity if coupling between the models is to be facillitated. Furthermore, circulation model applications are typically executed with marginal horizontal resolution commensurate with available computational resources. If one were to add frequency as an additional independent variable, with, say, 30 frequency bins and then add additional time for the computation of wave-wave interaction and integration of various properties including new coupling terms (M03, M05) one is faced with about a two order of magnitude increase in computational effort over that required by circulation models cum sole. Thus it does not seem practical to couple with wave models such as WAM (WAMDI Group 1988, Komen et al. 1994), WAVEWATCH (Tolman 1991) or SWAN (Booij and Holthuijsen 1999). At the other extreme is the very simple GLERL model (Schwab et al. 1984 - originally devised by Donelan 1977). Despite its simplicity the GLERL model has been shown to be relatively consistent with observations in several studies (Schwab et al. 1984, Lin et al. 2002). However, that model precludes shallow water effects, refraction, explicit wave dissipation and exchange of current and Stokes drift momentum.

Here, in order to include these attributes, we have developed a model that borrows a feature of the GLERL wave model and other models (SWAMP group 1985) in that the energy distribution in frequency space is parameterized using, in the present model, the spectrum by Donelan et al. (1985), henceforth DHH85, and which contains some elements of the JONSWAP spectrum (Hasselmann et al. 1973). This will . Thus, we will pursue an intermediate wave model (IWAM), which parameterizes the frequency wave distribution be computationally economical will avoid dealing with the wave-wave interaction process, and have the same level of complexity as circulation models - circulation models invoke the four independent variables, x,y,z,t and this wave model will use x, y, θ, t. The wave propagation angle, θ, will account for refraction due to bottom depth and current variations. For several code development reasons, it will be considerably easier to couple this model, compared to the aforementioned third generation models, to a circulation model. Another motivation is to directly confront unresolved research issues. For example, in M03 and M05, it was seen that some or all of the momentum transfer to the immediately underlying surface boundary layer is due to pressure transfer; surface boundary layer models generally assume that momentum transfer into the water column is entirely due to turbulence mixing coefficients. Of course, constraining to a specific spectral shape will incur some error in the general case of mixed seas and swell; lost accuracy in, say, the prediction of significant wave height and other integral wave properties remains to be determined.

We face a persistent and common dilemma: whether to define wave age as c_p/U_{10} or c_p/u_* where c_p is the phase speed at the peak of the wave spectrum; U_{10} is the wind speed at 10 m above the sea surface and u_* is the friction speed. Since the main parameter in the spectrum according to DHH85 is c_p/U_{10}, we will generally follow the same practice. Alves et al. (2003) offers evidence that c_p/U_{10} is the preferable wage age descriptor and from a practical point of view u_* is difficult to measure, but the issue does remain uncertain.

In this Part I paper, we develop the wave model *cum sole*. Part II will consider applications to spatially homogeneous fields where the focus will be on the coupling and interaction of wind driven waves and the wind and buoyancy driven surface boundary layer including the turbulence kinetic energy budget. Part III will test the complete coupled wave and circulation models against laboratory and field data.

Let $E_{\sigma\theta} = E_{\sigma\theta}(x, y, t, \sigma, \theta)$ be the directional spectrum, a function of x, y, t, a point in horizontal space and time, and σ, θ, the frequency and wave direction. (Henceforth, the arguments x, y, t will be deleted.) In this paper we will deal only with

$$E_\theta \equiv \int_0^\infty E_{\sigma\theta} d\sigma \tag{1a}$$

and since the kinetic and potential energies are equal

$$E_T = g\overline{\tilde{\eta}^2} = \int_{-\pi}^{\pi} E_\theta d\theta \tag{1b}$$

is the total wave energy per unit surface area, the product of the gravity constant and phase averaged, squared wave elevation summed over all frequencies and directions. We restrict our attention to surface gravity waves; i.e. wavelengths in excess of about 10 cm.

2. Monochromatic equations and definitions

We first define terms for a monochromatic wave field pursuant to dealing with spectra as a function of frequency and wave propagation angle.

From linear theory we have,

$$\omega = \sigma + k_\alpha u_{A\alpha}, \quad \sigma^2 = gk \tanh kD, \quad c = \sigma / k \qquad \text{(2a, b, c)}$$

where $k_\alpha = k(\cos\theta, \sin\theta)$ is the wave number vector, $k = |k_\alpha|$; θ is the wave propagation direction relative to the eastward direction; σ is the intrinsic frequency; the Doppler velocity, $u_{A\alpha}$, will be defined below; c is the phase speed; $D = h + \hat{\eta}$ is the water column depth where $\hat{\eta}$ is the mean surface elevation and h is the bottom depth; the superposed carat denotes mean (phase averaged) variables. The group velocity is

$$c_g = \frac{\partial \sigma}{\partial k} = cn, \quad n = \frac{1}{2} + \frac{kD}{\sinh 2kD}, \qquad c_{g\alpha} = \frac{k_\alpha}{k} c_g, \qquad \text{(3a, b, c)}$$

For the present wave model, (2b) is initially solved iteratively, inverted and cast in the form $kD = f_1(\sigma^2 D / g)$, and from (3b), $n = f_2(\sigma^2 D / g)$. A look-up table with interpolation comprises a subroutine in the code.

As cited in Komen et al. (1994), the refraction speed is $c_\theta = -|\nabla_h \omega \times \mathbf{k}| / k^2$ where ω is obtained from (2a). Working out the vector algebra (Golding 1978) yields

$$c_\theta = \frac{g}{2c\cosh^2 kD}\left[\sin\theta \frac{\partial D}{\partial x} - \cos\theta \frac{\partial D}{\partial y}\right] + \frac{k_\alpha}{k}\left[\sin\theta \frac{\partial u_{A\alpha}}{\partial x} - \cos\theta \frac{\partial u_{A\alpha}}{\partial y}\right] \qquad (4)$$

Before defining more terms, useful combinations of hyperbolic sines and cosines are,

$$F_{SS} = \frac{\sinh kD(1+\varsigma)}{\sinh kD}, \quad F_{CS} = \frac{\cosh kD(1+\varsigma)}{\sinh kD} \qquad \text{(5a, b)}$$

$$F_{SC} = \frac{\sinh kD(1+\varsigma)}{\cosh kD}, \quad F_{CC} = \frac{\cosh kD(1+\varsigma)}{\cosh kD} \qquad \text{(5c, d)}$$

The "sigma" variable is $\varsigma = (z - \hat{\eta}) / D$ (reserving σ for frequency) and it ranges from 0 at the mean sea surface $(z = \hat{\eta})$ to -1 at the bottom $(z = -h)$. A Doppler velocity is required for the wave energy equation and, and as described in M03, is

$$u_{A\alpha} = \int_{-1}^{0} U_\alpha \left(\partial F_{SS} F_{CC} / \partial \varsigma\right) d\varsigma \qquad (6)$$

where $U_\alpha = U_\alpha(x, y, \varsigma, t)$ is the ocean current. The wave radiation stress terms are

$$S_{\alpha\beta} = kDE\left[\frac{k_\alpha k_\beta}{k^2} F_{CS} F_{CC} + \delta_{\alpha\beta}(F_{CS} F_{CC} - F_{SS} F_{CS}\right] \qquad \text{(7a)}$$

$$S_{p\alpha} \equiv (F_{CC} - F_{SS})\left[\frac{F_{SS}}{2}\frac{\partial E}{\partial x_\alpha} + (1+\varsigma) F_{CS} E \frac{\partial kD}{\partial x_\alpha}\right] \qquad \text{(7b)}$$

When vertically integrated, $\int_{-1}^{0} S_{\alpha\beta} d\varsigma = E\left[(k_\alpha k_\beta / k^2)\left(c_g / c\right) + \delta_{\alpha\beta}\left(c_g / c - 1/2\right)\right]$ as in Phillips (1977).

3. The wave energy equation and description and the specified spectrum

After integrating the full spectral equation (a function of frequency and wave angle) with respect to frequency, we arrive at

$$\frac{\partial E_\theta}{\partial t} + \frac{\partial}{\partial x_\alpha}\left[\left(\bar{c}_{g\alpha} + \bar{u}_{A\alpha}\right)E_\theta\right] + \frac{\partial}{\partial \theta}[\bar{c}_\theta E_\theta] + \int_{-1}^{0} \bar{S}_{\alpha\beta} \frac{\partial U_\alpha}{\partial x_\beta} d\varsigma - \int_{-1}^{0} \bar{S}_{p\alpha} \frac{\partial U_\alpha}{\partial \varsigma} d\varsigma$$
$$= S_{\theta\, in} - S_{\theta\, Sdis} - S_{\theta\, Bdis} \qquad (8)$$

The horizontal coordinates are denoted by $x_\alpha = (x, y)$. The overbars represent spectral averages (and differ from the phase averaging usage in M03). The first two terms on the left of (8) determine the propagation of wave energy in time and horizontal space whereas the third term is the refraction term accounting for the change in direction of wave energy. The last two terms on the left include wave radiation stress terms, $\bar{S}_{\alpha\beta}$ and $\bar{S}_{p\alpha}$ representing energy exchange with the mean velocity energy equation as demonstrated in M05. All of the terms on the right of (8) are functions of θ. $S_{\theta\, in}$ is the wave energy source term dependent on wind properties. $S_{\theta\, Sdis}$ and $S_{\theta\, Bdis}$ are wave dissipation due to wave processes at the surface and bottom respectively. All terms are energy terms divided by water density. Thus the atmospheric work done on the water is $\rho_w S_{\theta\, in}$ where ρ_w is the seawater density. The terms, $\bar{c}_{g\alpha}, \bar{c}_\theta, \bar{u}_{A\alpha}, \bar{S}_{\alpha\beta}$ and $\bar{S}_{p\alpha}$ differ from their counterpart terms in section 2 in that they have been spectrally averaged. More details follow below.

Following DHH85, we stipulate

$$E_{\sigma\theta} = \alpha g^3 \sigma^{-4} \sigma_p^{-1} \exp\left[-\left(\frac{\sigma}{\sigma_p}\right)^{-4}\right] \gamma^{\exp\left\{-(\sigma-\sigma_p)^2/(2\sigma_{pw}^2\sigma_p^2)\right\}} \frac{\beta}{2} \operatorname{sech}^2\left[\beta(\theta - \bar{\theta})\right] \qquad (9)$$

Frequency is σ and σ_p is the peak frequency where $E_{\sigma\theta}$ is maximum; θ is the wave propagation direction; $\overline{\theta}$ is the mean wave propagation angle. The parameters in (9) are wave age dependent such that

$$\alpha = 0.006\left[U_c / c_p\right]^{0.55}, \quad \gamma = 1.7 + 6.0\log_{10}\left[U_c / c_p\right], \quad \sigma_{pw} = 0.08\left[1 + 4(U_c / c_p)^{-3}\right]$$

$$\beta = \begin{cases} 2.44(\sigma / 0.95\sigma_p)^{+1.3}; \; 0.56 < \sigma / \sigma_p < 0.95 \\ 2.44(\sigma / 0.95\sigma_p)^{-1.3}; \; 0.95 < \sigma / \sigma_p < 1.6 \\ 1.24; \quad \text{otherwise} \end{cases}$$

and $U_c = U_{10}\cos(\theta_w - \overline{\theta})$; U_{10} is the wind speed evaluated at the 10 m height and θ_w is the wind angle. The observations in DHH85 showed that $\overline{\theta}$ can differ from θ_w. In this model building process, we will use (9) as a weighting function where, however, retention or neglect of the difference between θ_w and $\overline{\theta}$ makes little difference in the calculated results; thus we set $U_c = U_{10}$. Using (9), various spectrally weighted averages were obtained by numerical integration. Following Terray et al. (1996) and Banner (1990), the spectra were extended beyond $3.5\sigma_p$ by appending a σ^{-5} tail to 20 σ_p whence the integration was terminated.

The total wave energy, E_T, according to (1a,b) and non-dimensionally in the form, $\sigma_p^4 E_T / g^3$, is plotted in Fig.1. This information can be simply described by

$$\sigma_p^4 E_T / g^3 = 0.00050 + 0.0015(U_{10} / c_p)^{1/2} + 0.00090\, U_{10} / c_p, \quad U_{10} / c_p > 0.45 \tag{10}$$

Eq. (10) will determine σ_p as a function of E_T and inverse wave age, U_{10} / c_p, as these quantities evolve. When $U_{10} / c_p < 0.45$, σ_p is unchanged from the previous value in the process of time stepping. The reason for the cutoff will be explained in section 5.

4. Spectrally averaged terms

Next we deal with terms that are predominantly independent of wave angle. For example,

$$\frac{\overline{c}_g}{c_p} = \frac{\int_0^\infty (c_g / c_p) E_{\sigma,\theta} d\sigma}{\int_0^\infty E_{\sigma,\theta} d\sigma} \tag{11a}$$

is, strictly speaking, a function of θ. However, a common approximation is that $E_{\sigma,\theta} = f(\theta)E_\sigma$. An examination of (9) shows that the two independent variables are not exactly separable, but, nevertheless, trials using (11a) show that the approximation is sufficiently accurate such that

$$\frac{\bar{c}_g}{c_p} = \frac{\int_0^\infty (c_g / c_p) E_\sigma d\sigma}{\int_0^\infty E_\sigma d\sigma} \tag{11b}$$

where $E_\sigma = \int_{-\pi/2}^{\pi/2} E_{\sigma,\theta} d\theta$. Similarly, integrations were carried out for other terms such that, in place of (4) and (7a,b), we have

$$\bar{c}_\theta = \frac{gF_{c\theta}}{2c_p \cosh^2 k_p D}\left[\sin\theta\frac{\partial D}{\partial x} - \cos\theta\frac{\partial D}{\partial y}\right] + \frac{k_\alpha}{k}\left[\sin\theta\frac{\partial \bar{u}_{A\alpha}}{\partial x} - \cos\theta\frac{\partial \bar{u}_{A\alpha}}{\partial y}\right] \tag{12a}$$

$$\bar{S}_{\alpha\beta} = E_\theta\left(\frac{k_\alpha k_\beta}{k^2}F_1 + \delta_{\alpha\beta}F_2\right) \tag{12b}$$

$$\bar{S}_{p\alpha} = F_3\frac{\partial E_\theta}{\partial x_\alpha} + F_4 E_\theta \frac{\partial k_p D}{\partial x_\alpha} \tag{12c}$$

$$\bar{u}_{A\alpha} = \int_{-1}^{0} U_\alpha (\partial F_5 / \partial \varsigma)\, d\varsigma \tag{12d}$$

In Fig. 2a, $\bar{c}_g / c_p$ and $F_{c\theta}$ are plotted as functions of $k_p D$. These variables are also dependent on inverse wave age, but the dependence is weak (a few percent) and will be neglected henceforth. For comparison, Eq. (3b) where kD is replaced by $k_p D$ is also plotted in Fig. 2a. All of the other $F_n{}'s$ in (12b, c, d) are explicitly defined in Appendix A and are functions of ς and $k_p D$ as shown in Fig. 2b for $U_{10} / c_p = 2$. The variations with respect to inverse wave age are small (in the range, $1 < U_{10} / c_p < 5$, mostly less than $\pm 5\%$ with a very few values near $\pm 10\%$) and henceforth neglected. Appendix A provides further information about these functions.

The wave-current interaction terms in (8) are complicated and a explicit record of the terms prior to coding is useful. Thus, using (12b,c)

$$\int_{-1}^{0} \overline{S}_{\alpha\beta} \frac{\partial U_\alpha}{\partial x_\beta} d\varsigma = E_\theta \left[\cos^2\theta \int_{-1}^{0} \frac{\partial U}{\partial x} F_1 d\varsigma + \int_{-1}^{0} \frac{\partial U}{\partial x} F_2 d\varsigma \right.$$

$$+ \cos\theta \sin\theta \int_{-1}^{0} \left(\frac{\partial U}{\partial y} + \frac{\partial V}{\partial x} \right) F_1 d\varsigma$$

$$\left. + \sin^2\theta \int_{-1}^{0} \frac{\partial V}{\partial y} F_1 d\varsigma + \int_{-1}^{0} \frac{\partial V}{\partial y} F_2 d\varsigma \right] \tag{13a}$$

$$\int_{-1}^{0} \overline{S}_{p\alpha} \frac{\partial U_\alpha}{\partial \varsigma} d\varsigma = \frac{\partial E_\theta}{\partial x} \int_{-1}^{0} \frac{\partial U}{\partial \varsigma} F_3 d\varsigma + E_\theta \frac{\partial k_p D}{\partial x} \int_{-1}^{0} \frac{\partial U}{\partial \varsigma} F_4 d\varsigma$$

$$+ \frac{\partial E_\theta}{\partial y} \int_{-1}^{0} \frac{\partial V}{\partial \varsigma} F_3 d\varsigma + E_\theta \frac{\partial k_p D}{\partial y} \int_{-1}^{0} \frac{\partial V}{\partial \varsigma} F_4 d\varsigma \tag{13b}$$

5. Wind growth source term

We next obtain $S_{\theta in}$ which can be written

$$S_{\theta in} = \int_0^\infty B_{\sigma\theta} E_{\sigma\theta} \, d\sigma \tag{14a}$$

$E_{\sigma\theta}$ is given by 9(a,b). The wave growth (Donelan 1999) is given by

$$B_{\sigma\theta} = 0.28 \frac{\rho_a}{\rho_w} \left| U(\lambda/2)\cos(\theta-\theta_w)/c - 1 \right| \left(U(\lambda/2)\cos(\theta-\theta_w)/c - 1 \right) \sigma \tag{14b}$$

where $U(\lambda / 2)$ is the wind speed evaluated at the half wave length height. Eq. (14b) has some similarity to an expression due to Janssen (1989) although he used the air side friction velocity u_{*a} instead of $U(\lambda / 2)$; the latter can be obtained from U_{10} using the law-of-the-wall according to

$$\frac{U(\lambda/2)}{U_{10}} = \frac{\ln(\lambda/2z_0)}{\ln(10\text{m}/z_0)} \ , \quad z_0 = 1.38 \times 10^{-4} H_S \left(\frac{U_{10}}{c_p} \right)^{2.66} \tag{15a, b}$$

$H_S = 4(E_T / g)^{1/2}$ (Longuet-Higgins 1952) is the significant wave height. Sample plots of $E_\sigma = \int_{-\pi}^{\pi} E_{\sigma\theta} d\theta$ using (9) and $B_\sigma = \int_{-\pi}^{\pi} B_{\sigma\theta} d\theta$ from (14b) are shown in Fig. 3. Thus it is seen that the wind source term is biased toward large frequencies since, for deep water, $c^{-1} = \sigma / g$ in (14b).

The friction velocity squared is

$$u_{*a}^2 = C_D |\delta \mathbf{U}|^2, \qquad C_D = \left(\frac{\kappa}{\ln(10m/z_0)} \right)^2 \tag{16a,b}$$

where $\delta \mathbf{U} = (U_{x,10} - U_{x,\varsigma=0}, U_{y,10} - U_{y,\varsigma=0})$ is the vector difference between the 10 meter wind velocity and the surface ocean current. The air side and water side friction velocities are u_{*a} and u_{*w} such that $\rho_w u_{*w}^2 = \rho_a u_{*a}^2$; $\rho_w / \rho_a = 860$ is the water to air density ratio and z_0 is obtained (Donelan 1990) from (15b).

Equation (14) was integrated to obtain the so-called spreading function, $f_{spr} = S_{\theta\, in} / S_{Tin}$, where $S_{Tin} = \int_{-\pi/2}^{\pi/2} S_{\theta\, in}\, d\theta$; the results are plotted in Fig. 4. The dashed line is

$$f_{spr} \equiv \begin{cases} \frac{\beta}{2} \operatorname{sech}^2[\beta(\theta - \theta_W)]; & |\theta - \theta_W| \le \pi/2 \\ 0 \quad ; & |\theta - \theta_W| > \pi/2 \end{cases} \tag{17a}$$

for $\beta = 2.2$ The spreading function is similar to that in (9) after replacing $\bar{\theta}$ with θ_w since the weighting function, used to find a local wave energy source term, $S_{\theta\, in}$, should depend on the local wind direction. As will be seen, the final model will produce calculations wherein $\bar{\theta}$ differs from θ_w due to non-local effects. In (17a), f_{spr} is quite small when $|\theta - \bar{\theta}| = \pi/2$; nevertheless, the cutoff for $|\theta - \bar{\theta}| > \pi/2$, improved the calculations in section 7 relative to data for small fetch.

After normalization by $c_p u_{*w}^2$, S_{Tin} is plotted versus wave age in Fig 5a. This is similar to the result obtained by Terray et al. (1996) who integrated $B_{\sigma\theta} E_{\sigma\theta}$ over frequency and angle; they also used (14b) but used observed spectra in place of (9) and naturally obtained more scatter than that of Fig. 5a. However, in their calculation, the constant, 0.28, in (14b) was replaced by 0.194 based on an estimate by Donelan and Pierson (1987) now updated to the present value estimated by Donelan (1999).

Another normalization, S_{Tin} / u_{*w}^3 versus U_{10} / c_p is plotted in Fig 5b. Noting that most of the wave energy source is directly dissipated into turbulence, values of $S_{Tin} / u_{*w}^3 = 100$ were empirically deduced by Craig and Banner (1994) and a value of 150 by Stacey (1999) in their treatments of the surface boundary layer. These values are consistent with young wave ages in Fig 5b. The dashed line in Fig. 5b is given by $S_{Tin}/u_{*w}^3 = 400\exp\left(-0.35U_{10}/c_p\right)$ but the calculated values abruptly decrease around $U_{10}/c_p = 0.45$ and become negative for lesser values. (When S_{Tin}/c_p^3 is plotted versus U_{10}/c_p the transition from positive to negative values is smooth and monotonic). This reversal in sign occurs when the wave speed exceeds the wind speed as manifest in Eq. (14b). If, for example, $U_{10} = 0$ after a history of finite wind then swell occurs and the spectrum given by (9) would hardly apply. Thus, we let

$$S_{\theta\, in}/u_{*w}^3 = \begin{cases} 400\exp\left(-0.35U_{10}/c_p\right)f_{spr}, & U_{10}/c_p > 0.45 \\ 0, & \text{otherwise} \end{cases} \tag{17b}$$

One effect of the cutoff at $U_{10}/c_p = 0.45$ is that, for zero wind speed, the waves will decay by e^{-1} in about a half day according to the dissipation described in section 6 and at a constant wave period prescribed by (10). We do not suggest that swell simulations are accurate under these conditions but nevertheless the resulting behavior should not significantly detract from overall model performance. Note that a fully developed wave field is often taken to be $U_{10}/c_p = 0.83$ although that is considered to be an approximate number.

The calculations leading to Figs. 4 and 5 and Eq. (17) were for deep water where $c = g/\sigma$. With a more complex algorithm, we have calculated the dependency of S_{Tin}/u_{*w}^3 on $k_p D$. The results are in Appendix C; the additional complexity of the added dependency is deemed not necessary.

An aside

As shown in M03 and after spectral averaging

$$S_{Tin} = c_\alpha \overline{\tilde{p}_{w\eta}\frac{\partial\tilde{\eta}}{\partial x_\alpha}} \quad \text{and} \quad \tau_{p\alpha}(0) = \overline{\tilde{p}_{w\eta}\frac{\partial\tilde{\eta}}{\partial x_\alpha}} \tag{18a, b}$$

where $\tau_{p\alpha}(0)$ is the surface momentum stress due to those components of the wind pressure fluctuation which are correlated with the surface wave slope. Based on (18a, b) and for a spectrum of waves, one might speculate that

$$\tilde{\tau}_p(0) = \left|\tilde{\tau}_{p\alpha}(0)\right| = \rho_w \int_{-\pi}^{\pi}\int_0^{\infty} c^{-1} B_{\sigma\theta} E_{\sigma\theta}\, d\sigma\, d\theta$$

so that, in fully rough flow cases ($U_{10} > 6\text{ms}^{-1}$), one might presume $\tau_p(0) = \rho_w u_{*w}^2$ to be equal to $\tilde{\tau}_p(0)$. However, calculations reveal that $\tilde{\tau}_p(0)$ is a fraction of that given by $\tau_p(0)$ depending on wave age, 36% for $U_{10}/c_p = 5.0$ and 22% for $U_{10}/c_p = 1.0$ (with just a $\pm 1\%$ variations of these fractions for a range of values from U_{10}= 10 ms^{-1} to 25 ms^{-1}). This discrepancy may be due to the use of observed frequency directional spectra, rather than wavenumber spectra, to evaluate Eq. (18).

Terray et al. (1996, 1997) obtained a plot similar to Fig. 5a but labeled the ordinate $\bar{c}/c_p$; then $\rho_w S_{Tin} = \bar{c}\,\tau_p(o) = \bar{c}\rho_w u_{*w}^2$ where $\bar{c}$ (the overbar differs from usage in this paper) is an "effective" wave speed which is then normalized by c_p.

6. Wave dissipation

The total wave dissipation must be determined empirically. A model for white capping or wave breaking is

$$S_{\theta Sdis} = aS_{\theta in} + bE_\theta \sigma_p \tag{19}$$

where *a* and *b* are to be determined. The first term represents the fact that the high frequency part of the spectrum is dissipated very nearly *in situ* and the second part is dissipation of the middle ($\sigma \approx \sigma_p$) to low frequency part of the spectrum. This means, of course, that overall wave growth only responds to $(1-a)S_{\theta in} - bE_\theta \sigma_p$; nevertheless, the full dissipation will be needed as input to the turbulence kinetic energy equation when the coupled wave, circulation model is invoked. (To the second term, we had thought to add a factor involving the wave slope in the form, $(k_p H_s)^p$, where $k_p H_s$ is nearly proportional to inverse wave age but results were fairly insensitive to *p* and, in fact, *p* = 0 provided a good result as shown below.) An estimate of *b* as a function of *a* may obtained by equating $S_{\theta Sdis} = S_{\theta in}$ for a fully developed sea when $U_{10}/c_p = 0.83$. Thus, dominant leverage on computed results are via the parameter, *a*, as determined in section 7.

In shallow water, one should add depth induced wave breaking terms to $S_{\theta Sdis}$ (Battjes and Jansen 1978) and the effects of bottom friction via the term, $S_{\theta Bdis}$ in Eq. (8).

7. Simple tests

All of the tests in this section are independent of the coordinate, *y*. In fact, there exists two codes, one whose independent variables are x, t and θ, used in this section, and another code whose independent variables are x, y, t and θ. The latter is used in section 8. Numerical details are in Appendix B.

Refraction for a monochromatic wave train

We first test the model against Snell's Law for the case, $U_\alpha = 0$ and $U_{10} = 0$. At *x* = 0, $E_\theta \propto (\beta/2)\mathrm{sech}^2\left[\beta(\theta-\theta_0)\right]$ where $\theta_0 = 60^{\circ}$ and $\beta = 4.0$, a rather narrow distribution with respect to θ. Equation (8) with a null right side is then solved to steady state. The time, spatial and angle increments are 20 s, 500m and $2\pi/24 = 15^{\circ}$ respectively.

The bottom topography is shown in Fig. 6a. The frequency is $\sigma = 2\pi/10s$; the corresponding $c(x)$ and $c_g(x)$ are plotted in Fig. 6b. The solution to Eq. (8) is given in Fig. 6c. Note that the angle domain is $-\pi < \theta < \pi$ but only the active portion is shown. In Fig. 6d, the total wave energy, $E_T = \sum_{k=1}^{2\pi/\Delta\theta} E_\theta(\theta_k)\Delta\theta$, and is normalized with its value at $x = 0$. The mean angle, $\bar{\theta} = \sum_{k=1}^{2\pi/\Delta\theta} \theta E_\theta(\theta_k)\Delta\theta / E$, is shown in Fig. 6e.

Calculations are obtained from Snell's law whence

$$\theta(x,m) = \sin^{-1}\left(c(x)\sin(\theta(0,m)/c(0)\right) \tag{20a}$$

$$E(x,m) = c_g(0)\cos\theta(0,m)E(0,k)/(c_g(x)\cos\theta(x,m)) \tag{20b}$$

and *m* is the label on each ray emanating from *x* = 0 where the initial distribution is as stated above. Averages are obtained on *m* and are plotted as the dashed lines in Figs. 6d and 6e. Agreement between model and Snell's law is improved further (the two curves are nearly indistinguishable) by decreasing the angle increment from 15° to 10°.

Fetch limited waves

The model was tested against the growth of waves for a constant offshore wind normal to a straight north-south coast located at x = 0. For this problem, Similarity growth relations were formulated by Kitaigorodskii (1962) using dimensional analysis. As reported in Komen et al. (1994, p.181), Kahma and Calkoen examined data from the JONSWAP experiment and data observed in the Bothnian Sea and Lake Ontario (DHH85). They first separated data into winds when the vertical density stratifications were stable or unstable. However, we deal only with the composite data set which they represented by

$$\frac{E_T g}{U_{10}^4} = 5.4 \times 10^{-7} \left(\frac{xg}{U_{10}^2} \right)^{0.9} \tag{21}$$

and which is plotted as a dashed line in Fig. 7. The well developed limit of $E_T g / U_{10}^4 = 3.6 \times 10^{-3}$ is from Pierson and Moskowitz (1964).

Another fit to Lake St. Clair data by Donelan et al. (1992), using an elaborate analysis scheme to minimize inhomogeneities in the data, is shown as a dot-dashed line in Fig. 7.

The solid lines are from the present model for two different values of U_{10} and for the adjustable parameters, a = 0.924, $b = 2.0 \times 10^{-5}$; these values are hereafter held constant. Whereas the data syntheses exclude dependence on U_{10}, there must be some model dependence on U_{10} or, in dimensionless form, $U_{10} /(g10\text{m})^{1/2}$ as seen from (10) and (15 b) and $H_S = 4(E/g)^{1/2}$. The time and angle increments are 10 s and 15$^{\text{o}}$ respectively; at x = 0, the spatial step is $\Delta x = 100\text{m}$ but subsequently $\Delta x(i+1) = 1.10 \Delta x(i)$.

In Fig. 8 we show calculations of the time and distance development of wave growth together with a synthesis of data by Hwang and Wang (2004). Since duration-limited data is scarce and difficult to obtain, they deduced duration-limited growth from fetch-limited growth and compared with their own and other data sets; a synthesis of their duration-limited data is also shown in Fig. 8. A comparison (not shown) of non-dimensional frequency, $\sigma_p U_{10} / g$, vs. xg / U_{10}^2 was also quite favorable.

In Fig. 9a, b we show the behavior for $U_{10} = 10\text{m}$ and for different wind angles relative to the eastward direction; the coastline is north-south at x = 0. For wind angles not equal to zero and, because of the spread of the wind growth term in (17) denoted by f_{spr} , waves with propagation angles larger than the wind angle will propagate over a longer fetch and therefore accrue higher energies than waves with lower angles; the mean wave angle therefore differs from the wind angle until a considerable distance from the coast where the two angles coincide. The mean wave angle is given by

$$\overline{\theta} = \tan^{-1}\left[\frac{\int_{-\pi}^{\pi} E_\theta \sin\theta \, d\theta}{\int_{-\pi}^{\pi} E_\theta \cos\theta \, d\theta}\right] \tag{22}$$

If E_θ is zero in the neighborhood of the branch cut at $-\pi, \pi$, a simple average yields very nearly the same result as (22).

For small wind angles, say $\theta_w = \pi / 6 = 30^o$, at the coast ($x$ =0) energy input near the wind angle is small since the effective fetch is small and the flow angle is dominated by wave propagation components around $\theta = 90^o$ corresponding to very large fetch. Consider the extreme case of wind parallel to the coast, $\theta_w = \pi / 2 = 90^o$. At the coast ($x$ = 0), the wind only produces waves in the range $0 < \theta < \pi / 2$ whereas, in the far field ($x \to \text{large}$), the wind produced the full range $0 < \theta < \pi$; thus the mean wind angle is larger and the energy smaller at the coast than the far field. Relatively, energy propagating from the far field to the coast is dissipated before reaching the coast.

Refraction due to Currents

A northward Gulf Stream like jet is prescribed according to

$$V = 2.0\text{ms}^{-1} \exp\left[\left(\frac{x - L/2}{50\text{km}}\right)^2\right] \exp\left[\frac{z}{1000\text{m}}\right] \tag{23}$$

where L = 400km is the domain zonal width. The spatial, temporal and angle increments are 5 km, 500s and 15$^\text{o}$ respectively. Since the waves are confined to the near surface, the depth dependence is not important in this application, but the code generally does account for depth dependence through the interaction terms in (8) and (12).

A background, fully developed wave field is first established in the absence of the jet with a wind speed of $U_{10} = 10\,\mathrm{m\,s^{-1}}$ and varying directions, northward (90^o) through southward (-90^o); wave energy and mean propagation angle are shown in Fig. 10 as dashed lines. Here, lateral boundary conditions are devised so that fully developed wave energy propagates through the domain boundaries. The mean propagation angles are the same as the wind direction.

With the jet in place, the solid curves in Fig. 10 show the deviations of wave energy and mean angle. Analysis of the calculations show that, in this application, the term $(k_\alpha / k)\sin\theta\, \partial \overline{u}_{A\alpha} / \partial x = \sin^2\theta\, \partial \overline{v}_A / \partial x$ in (12a) where $\overline{v}_A \equiv \overline{u}_{Ay}$, evaluated through (12d), is mostly responsible for the current induced deviations.

8. The x, y, θ, t model

Heretofore, for computational efficiency, we have used a x, θ, t model**.** The same model but with the added dependency on y is now invoked. The grid may be an orthogonal, curvilinear grid, but for this paper we will specialize to a more conventional rectilinear grid.

We leave it to a future paper to compare the model with specific field campaigns (although Figs. 7 and 8 include syntheses of many field data). We adopt the simple case of an elliptical basin as did Donelan (1980) with the quite elongated major to minor axis ratio of 4.50 and length of 304 km. (This idealized basin is roughly similar to Lake Ontario.) The model is forced with a wind speed of 10 m s^{-1} and different wind angles relative to the basin's major axis direction. Fig. 11 shows the resultant significant wave heights and wave angle deviation for the wind angle of 120^o. This produced the largest deviation whereas the deviations for a 0^o and 180^o wind were nil. The calculations are shown near the western shore where the telescoping grid is the finest. Grid spacing in the east-west direction begins at 200 m increasing by 10% until 8.53 km after which the spacing is held constant until reaching the western shore of the ellipse. In the north-south direction the grid spacing starts at 204 m at the centerline and increases by 10% outward.

At a distance of 3.28 km from the western shoreline and on the centerline, the focal point of the ellipse, the angle deviations are only about 40% of that deduced by Donelan (1980) for the directional deviation (from the wind direction) of the waves at the spectral peak. This is to be expected because the short waves tend to line up with the wind; i.e. vanishing directional deviation, so that the average directional deviation predicted with this model is less than the value at the peak (as described by Donelan, 1980). Increasing the wind speed to 20 ms^{-1} brings closer agreement because the increased forcing causes increased peak enhancement and therefore closer agreement with the peak direction. To avoid much of the staircase effect along the southern coast, a curvilinear grid could be created that would conform more nearly to the coastline.

9. Summary

A new surface wave model has been developed; it includes depth dependent wave-current interaction terms in both the wave energy equation (and the ocean circulation equations) derived by M03. It is a stand-alone model but it is designed so that coupling with circulation models will be simple and numerically efficient. Model calculations compare favorably with established fetch and duration "laws". The next step will be to couple the model with a one-dimensional surface boundary layer model to investigate the interplay between vertical momentum transfer due to pressure and that due to turbulence as formulated in M03 and M05.

Acknowledgements. Some of this research was conducted while GLM was a visiting professor at the Technical University of Delft; he is indebted to the staff of the Fluid Mechanics Section for valuable consultation. GLM was funded by the NOPP surf-zone project and by ONR Grant N0014-01-1-0170.

Appendix A:

For (12a), we have

$$F_{c\theta}(k_p D) = E_T^{-1} \int_0^\infty E_\sigma \frac{c_\theta}{c_p} \left(\frac{\cosh k_p D}{\cosh kD} \right)^2 d\sigma \qquad \text{(A1)}$$

For (12b) we have

$$F_1(k_pD,\varsigma) = E_T^{-1}\int_0^\infty E_\sigma kDF_{CS}F_{CC}d\sigma \tag{A2a}$$

$$F_2(k_pD,\varsigma) = E_T^{-1}\int_0^\infty E_\sigma kDF_{CS}(F_{CC}-F_{SS})d\sigma \tag{A2b}$$

For (12c), we have

$$F_3(k_pD,\varsigma) = E_T^{-1}\int_0^\infty E_\sigma (F_{SS}/2)(F_{CC}-F_{SS})d\sigma \tag{A3a}$$

$$F_4(k_pD,\varsigma) = E_T^{-1}\int_0^\infty E_\sigma (1+\varsigma)F_{CS}(F_{CC}-F_{SS})d\sigma \tag{A3b}$$

For (12d)

$$F_5 = E_T^{-1}\int_0^\infty E_\sigma F_{CC}F_{SS}d\sigma \tag{A4}$$

The behavior of the various functions is useful to check the numerical calculations and to extend the numerical results for large and small k_pD. First the monochromatic functions behave as follows:

$kD \rightarrow$	0	∞
F_{SS}	$1+\varsigma$	$\exp(kD\varsigma)$
F_{SS}	$1/kD$	$\exp(kD\varsigma)$
F_{CC}	1	$\exp(kD\varsigma)$

The behavior of the spectrally averaged functions obtained by numerical integration are as follows:

$k_pD \rightarrow$	0	∞
F_1	1	$1.60k_pD\exp(4.74k_pD\varsigma)$
F_2	$-\varsigma$	0
F_3	$-\varsigma(1+\varsigma)/2$	0
F_4	$-\varsigma(1+\varsigma)/(k_pD)$	0
F_5	$1+\varsigma$	$\exp(2.89k_pD\varsigma)$

The constants in $F_1(k_p D \to \infty)$ and $F_5(k_p D \to \infty)$ are obtained from an fit to the calculations at the two topmost points, $\varsigma = 0.0$ and 0.05. For monochromatic waves, we would simply have $kD\ \exp(\ 2kD\ \varsigma\ )$ and $\exp(2kD\varsigma)$ respectively.

A look-up table was prepared using numerical integrations for $k_p D = 0.2, 0.4, \cdot, \cdot, \cdot, 3.0, 100.0$.

For $k_p D \geq 3.0$, all of the functions in (5) revert to simple exponentials dependent on $k_p D$ and $k_p z$ and some terms in (7) are nil. The result is that $F_1(k_p D, k_p z) = (k_p D / 100) F_1(100, k_p z)$, $F_5(k_p D, k_p z) = F_5(100, k_p z)$ and $F_2 = F_3 = F_4 = 0$. These rules are verified by the numerical integrations for $k_p D = 3.0$.

Appendix B: Some numerical details

The following code will accommodate an orthogonal curvilinear grid in *x, y* space in the sense of a finite volume. The leap-frog tendency term is split so that

$$\Delta x \Delta y \frac{\tilde{e}_{i,j,m} - e^{n-1}_{i,j,m}}{2\Delta t} + F^n_{X,i+1,j,m} - F^n_{X,i,j,m} + F^n_{Y,i,j+1,m} - F^n_{Y,i,j,m} = 0 \qquad \text{(B-1)}$$

where

$$F^n_{X,i,j,m} = \left[0.5 c_{gx,i,j,m}(e^n_{i,j,m} + e^n_{i-1,j,m}) - \gamma \left| c_{gx,i,j,m} \right| (e^{n-1}_{i,j,m} - e^{n-1}_{i-1,j,m})\right] \overline{\Delta y} \qquad \text{(B-2a)}$$

$$F^n_{Y,i,j,m} = \left[0.5 c_{gy,i,j,m}(e^n_{i,j,m} + e^n_{i,j-1,m)}) - \gamma \left| c_{gy,i,j,m} \right| (e^{n--1}_{i,j,m} - e^{n-1}_{i,j-1,m})\right] \overline{\Delta x} \qquad \text{(B-2b)}$$

The orthogonal cell dimensions are Δx and Δy reckoned at the cell center; they may vary cell to cell according to a particular curvilinear grid. The group velocity components and $\overline{\Delta x}$ and $\overline{\Delta y}$ are located at the edge of each cell. After executing (B-1), $\tilde{e}_{i,j,m} = \max(\tilde{e}_{i,j,m}, 1 \times 10^{-5})$; the lower limit corresponds to $H_S = 1\ \text{mm}$.

The terms modified by the γ coefficient are diffusion-like terms. For $\gamma = 0$, the result is pure central differencing whereas, for $\gamma = 0.5$, the result is pure upwind. Most calculations in the main text used $\gamma = 0.2$. However at cells adjacent to boundaries we stipulate local up-winding by setting $\gamma = 0.5$. For the elliptical basin problem using

$\gamma = 0.2$ (except on adjacent boundary points) resulted in small calculated oscillations very near the western boundary; the oscillations disappeared for $\gamma = 0.5$. In general, however, the difference in calculated results between the two values of γ were very small.

The time step in angle space is

$$\frac{\hat{e}_{i,j,m} - \tilde{e}_{i,j,m}}{2\Delta t} + \frac{F^n_{\theta,i,j,m+1} - F^n_{\theta,i,j,m}}{\Delta\theta} = D \tag{B-3}$$

where

$$F^n_{\theta,i,j,m} = 0.5\left(c_{\theta,i,j,m} + \left|c_{\theta,i,j,m}\right|\right) e^n_{i,j,m-1} + 0.5\left(c_{\theta,i,j,m} - \left|c_{\theta,i,j,m}\right|\right) e^n_{i,j,m} \tag{B-4}$$

Initially $D = 0$ so that (B-3) and (B-4) combine for a pure upwind differencing and positive definite algorithm. However, following Smolarkiewicz (1984), the solution is iterated such that an anti-diffusion *D* is calculated to reduce the diffusion incurred by upwinding; it is inserted into (B-3) for each iterant while maintaining positive definiteness. In practice, three iterations are sufficient after which negligible change is obtained. For the details in calculating *D*, the reader is referred to the paper by Smolarkiewicz. A grid stencil, emphasizing the angle grid, is shown in Fig. 12. The angle space is $-\pi$ to $+\pi$. Cyclic boundary conditions connect the branch cut at $-\pi, \pi$.

Finally the source terms, (17) and (18), are included such that

$$\frac{e^{n+1}_{i,j,m} - \hat{e}_{i,j,m}}{2\Delta t} = A + B e^{n+1}_{i,j,m} \tag{B-5}$$

so that the part of $S_{\theta\,in} + S_{\theta\,dis} = A + B e^{n+1}_{i,j,m}$ that is dependent on $e_{i,j,m}$ is executed implicitly.

Appendix C:

The non-dimensional form of (9) is $\sigma_p^5 E_{\sigma\theta} / g^3$ and that of (14b) is $B_{\sigma\theta} / \sigma_p$ whence (14a) may be written

$$\frac{\sigma_p^3 S_{\theta\,in}}{g^3} = \int_0^\infty \frac{B}{\sigma_p} \frac{\sigma_p^5 E_{\sigma\theta}}{g^3} d(\sigma / \sigma_p) \tag{C1}$$

Plots of $\sigma_p^3 S_{\theta\,in} / g^3$ as functions of inverse wave age and wind speed are shown in Fig. 13. For all practical purposes, dependence on $k_p D$ can be ignored. However, when renormalized as in Fig. 5b, we have, after some algebra

$$\frac{S_{\theta\, in}}{u_*^3} = \frac{\sigma_p^3 S_{\theta\, in}}{g^3}\left(\frac{g}{\sigma_p c_p}\right)^3\left(\frac{c_p}{U_{10}}\right)^3\left(\frac{\rho_w}{\rho_a C_D}\right)^{3/2}$$

or

$$\frac{S_{\theta\, in}}{u_*^3} = \frac{\sigma_p^3 S_{\theta\, in}}{g^3}\left(\frac{c_p}{U_{10}}\right)^3\left(\frac{\rho_w}{\rho_a C_D}\right)^{3/2}\left(\frac{1}{\tanh k_p D}\right)^3 \quad \text{(C2)}$$

The dependence on wave age and wind speed is manifest in the first three factors on the right of (C2) whereas, in the fourth factor, the dependence on $k_p D$ is weak for $k_p D > 2$, but for $k_p D$ less than unity, $(\tan k_p D)^{-3} \cong (k_p D)^{-3}$; presumably breaking occurs before small values of $k_p D$ are obtained.

References

Alves, J. H. G. M., M. L. Banner and I. R. Young, 2003: Revisiting the Pierson-Moskowitz asymptotic limits for fully developed wind waves. *J. Phys. Oceanogr*, 33, 1301-1323.

Banner, M. L., 1990: Equilibrium spectra of wind waves. *J. Phys. Oceanogr.*, **20,** 966-984

Battjes, J. A. and J. P. F. M. Janssen, 1978: Energy loss and set-up due to breaking of random waves. *Proceedings of the 16th International Conference of Coastal Engineering*, Am. Soc. of Civ. Eng., New York, 569-587.

Booij, N. and R. C. R. H. Holthuijsen, 1999: A third generation wave model for coastal regions, 1. Model description and validation. *J. Geophys. Res.*, **104,** 7649-7666.

Craig, P. D. and M. L. Banner, 1994: Modeling wave-enhanced turbulence in the ocean surface layer. *J. Phys. Oceanogr.*, **24,** 2546-2559.

Donelan, M. A., 1977: A simple numerical model for wave and wind stress prediction. Report, Nat. Water Res. Inst., Burlington Ont.

Donelan, M. A., 1980: Similarity theory applied to the forecasting of wave heights, periods and directions. *Canadian Coastal Conference*, Burlington, Ontario.

Donelan, M. A., J. Hamilton, and W. H. Hui, 1985: Directional spectra of wind-generated waves. *Phil. Trans. Roy. Soc. Lond. A*, **315,** 509-562.

Donelan, M. A. and W. J. Pierson, 1987: Radar scattering and equilibrium ranges in wind generated waves with application to scatterometry. *J. Geophys. Res.*, **92,** 4971-5029.

Donelan, M.A., 1990: Air-sea interaction. In *The Sea: Ocean Engineering Science*, **9**, 239-292.

Donelan, M., M. Skafel, H. Graber, P.Liu, D.Schwab, and S. Venkates, 1992: On the growth of wind-generated waves. *Atmosphere-Ocean*, **30,** 457-478.

Donelan, M. A., 1999: Wind-induced growth and attenuation of laboratory waves. Proceedings edited by S. G. Sajjadi, N. H. Thomas and J. C. R. Hunt, *Wind-over-Wave Couplings*, Clarendon Press, 183-194.

Golding, B.W., 1978: A depth dependent wave model for operational forecasting. *Turbulent Fluxes through the Sea Surface, Wave Dynamics and Prediction*, A. Favre and K. Hasselmann, Ed., Plenum Press, 593-604.

Hasselmann, K., T. P. Barnett, E. Bouws, H. Carlson, D. E. Cartwright, K. Enke, J. A. Ewing, H. Gienapp, D. E. Hasselmann, P. Kruseman, A. Meerburg, P. Muller, D. J. Olbers, K. Richter, W. Sell, and H. Walden, 1973: Measurements of wind-wave growth and swell decay during the Joint North Sea Wave Project (JONSWAP). *Dt. Hydrogr. Z.*, **A8 (Suppl.), no 12,** 95p.

Hwang, P. A. and D. W. Wang, 2004: Field measurementsof duration-limited growth of wind-generated ocean surface waves at young stage of development. *J. Phys. Oceanogr.*, **34,** 2316-2326.

Janssen, P. A. E. M., 1989: Wave induced stress and drag of air over sea water. *J. Phys. Oceanogr.*, **19,** 1631-1642.

Longuet-Higgins, M. S., 1952: On the statiscal distribution of the heights of sea waves. *J. Mar. Res.*, **XI,** 245-266.

Kitaigorodskii, S. A., 1962: Application of the theory of similarity to the analysis of wind-generated water waves as a stochastic process. *Bull. Acad. Sci. USSR Ser.* no. 1**,** 73p.

Komen, G. J., L. Cavaleri, M. Donelan, K. Hasselmann, S. Hasselmann, and P. A. E. M. Janssen, 1994: *Dynamics and Modelling of Ocean Waves*. Cambridge University Press.

Lin, W., L. P. Sanford, and S. E. Suttles, 2002: Wave measurements and modeling in Chesepeake Bay. *Continental Shelf Res.*, **22,** 2673-2686.

Mellor, G. L., 2003: The three dimensional, current and surface wave equations. *J. Phys. Oceanogr.*, **33,** 1978-1989.

Mellor, G. L., 2005: Some consequences of the three-dimensional current and surface wave equations. *J. Phys. Oceanogr.*, In Press

Phillips, O. M., 1977: *The Dynamics of the Upper Ocean, Cambridge University*. Cambridge University Press, Cambridge, 336 pp

Pierson, W. J. and L. Moskowitz, 1964: A proposed spectral form for fully developed wind seas based on the similarity theory of A. A. Kitaigoradskii. *J. Geophys. Res.*, **69,** 5181-5190.

Schwab, D. J., J. R. Bennett, P. C. Liu and M.A. Donelan, 1984: Application of a simple numerical wave prediction model to Lake Erie. *J. Geophys. Res.*, **89,** 3586-3592.

SWAMP group, 1985: *Ocean Wave Modeling*. Plenum Press, New York and London, 256 pp.

Stacey, M. W., 1999: Simulations of the wind-forced near-surface circulation in Knight Inlet: a parameterization of the roughness length. *J. Phys. Oceanogr.*, **29,** 1363-1367.

Terray, E. A., M. A. Donelan, Y. C. Agrawal, W. M. Drennan, K. K. Kahma, A. J. W. Williams III, P. A. Hwang, and S. A. Kitaigorodski, 1996: Estimates of kinetic energy dissipation under breaking waves. *J. Phys. Oceanogr.*, **26,** 792-807.

Terray, E. A., M. A. Donelan, Y. C. Agrawal, W. M. Drennan, K. K. Kahma, A. J. W. Williams III, P. A. Hwang, and S. A. Kitaigorodski, 1997: Reply. *J. Phy. Oceanogr.*, **27,** 2308- 2309.

Tolman, H. L., 1991: A third-generation model for wind waves on slowly varying, unsteady, and inhomogeneous depths and currents. *J. Phys. Oceanogr.*, **21,** 782-797.

WAMDI Group, 1988: The WAM model - A third generation ocean wave prediction model. *J. Phys. Oceanogr.*, **18,** 1775-1810.

Figure Captions

Fig.1. The inverse wave age dependence of the relation between peak frequency and total wave energy. The dashed line is from Eq. (10). It is thought that fully developed wave fields correspond to $U_{10}/c_p \cong 0.83$.

Fig.2. (a) The solid curves are spectrally weighted values of phase $\bar{c}_g / c_p$ and $F_{c\theta}$ as functions of $k_p D$. The dashed curve is from (3b). Wave age dependencies are small and are ignored in the model. (b) Spectrally weighted values of F_n for $k_p D$ = 0.2, 1.0, 2.0 and 3.0.

Fig. 3. A plot of the non-dimensional DHH85 spectrum, Eq. (9), and the wave growth relation, Eq. (14b), as function of frequency for $U_{10} / c_p = 2.0$.

Fig. 4. The directional distribution of wind energy input as functions of relative wave propagation angle, wind speed and wave age (the closely packed curves with no labels). The dependencies on wind speed and wave age are neglected in the model. The dependence on propagation angle are simply described by (9b) (for $\beta = 2.2$ and $\bar{\theta}$ is replaced by θ_w), which is plotted as the dashed curves.

Fig. 5. (a) The wind energy source term normalized on $c_p u_{*w}^2$ vs. u_{*a}/c_p as plotted by Terray ett al. (1997). (b) The same wind energy source but normalized on u_{*w}^3 vs. U_{10}/c_p which is a convenient form for the wave model.. In both plots the ascending curves are for U_{10} = 10, 20 and 30 ms^{-1} respectively. The dashed line is from (17) integrated over all angles and is used in the model.

Fig. 6. A simple test of refraction wherein calculations from Eq. (2) are compared with Snell's Law for a wave period of 10 s. (a) the bottom topography. (b) the phase and group speed. (c) the distribution of wave energy in propagation angle and distance space. (d) the

angle integrated (total) wave energy calculated (solid line) and for constant energy flux (dashed line). (e) the mean wave propagation angle as calculated (solid line) from Snell's Law (dashed line). The grid spacing is $\Delta x = 0.5\,\mathrm{km}$ and $\Delta\theta = 15^o$.

Fig.7. The calculated fetch dependent wave energy versus non-dimensional fetch distance. Calculations for $U_{10} = 10$ and $20\mathrm{ms}^{-1}$ (solid lines) are compared with Eq. (21) (dashed line) and a result from Donelan et al. (1992) (dot-dashed line). The later two curves represent a synthesis of observational data for a range of wind speeds. The wind angle is normal to the coast located at $x = 0$.

Fig.8. The calculated fetch dependent wave energy versus non-dimensional fetch distance and duration for $U_{10} = 10\ \mathrm{ms}^{-1}$. For $U_{10} = 20\mathrm{ms}^{-1}$, the calculated values would be offset vertically as in Fig. 7. The O s are fetch limited estimates from Hwang and Wang (2004, Fig. 5) The X s are duration limited estimates from the same source. See their paper for data scatter which is greatest for large values of non-dimensional x and t.

Fig. 9. (a) The same as Fig.7 for a wind speed of $U_{10} = 10\mathrm{ms}^{-1}$ and for different mean wind angles relative to the normal to the coast at $x = 0$. (b) A plot of the mean wave propagation angle, defined by (22), versus fetch.

Fig. 10. The influence of a northward Gulf Stream like jet (maximum velocity = 2 m s^{-1}) on waves forced by 10 m s^{-1} winds whose angle varies from 90^o (northward; wind and jet velocities in the same direction) to -90^o (southward; wind and jet velocities in opposite directions). (a) The variation of wave energy. The dashed line is the background fully developed wave field in the absence of the jet. (b) The variation of the mean propagation angle for the same mean wind angles as in (a).

Fig.11. Calculations for an elliptical basin (only the western portion is shown) forced by a wind speed of 10 m s^{-1} and at 120^o from the eastward direction as shown by the arrow insert. The cross identifies a location of 3.8 km from the western shore and the focal point

of the ellipse. (a) the significant wave height; contour spacing is 10 cm. (b) deviation of the mean wave propagation angle from the wind direction; the contour spacing is 2^{o}.

Fig. 12. The computational stencil emphasizing the propagation angle grid and the cyclic boundary conditions. Wave energy, $e_{i,j,m}$, is located at the center of each cell and the speeds, $c_{gx,i,j,m}$, $c_{gy,i,j,m}$ and $c_{\theta,i,j,m}$, are located at the edge of each cell.

Fig. 13. The non-dimensional group, $\sigma_p^3 S_{in} / g^3$ as a function of inverse wave age, wind speed and $k_p D$ as labeled on each curve.

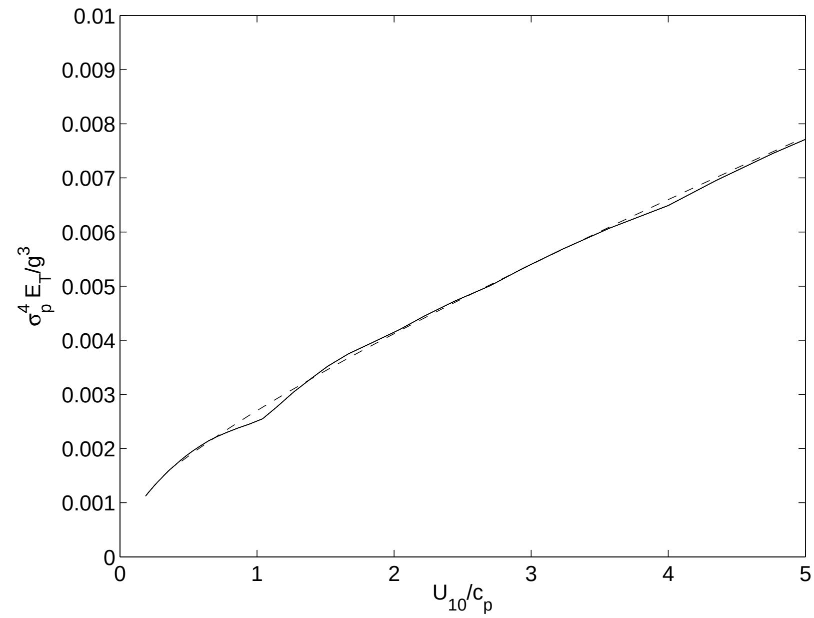

0.01
0.009
0.008
0.007
0.006
0.005
0.004
0.003
0.002
0.001
0
$\sigma_p^4 E_T/g^3$
0
1
2
3
4
5
U_{10}/c_p

Fig. 1.

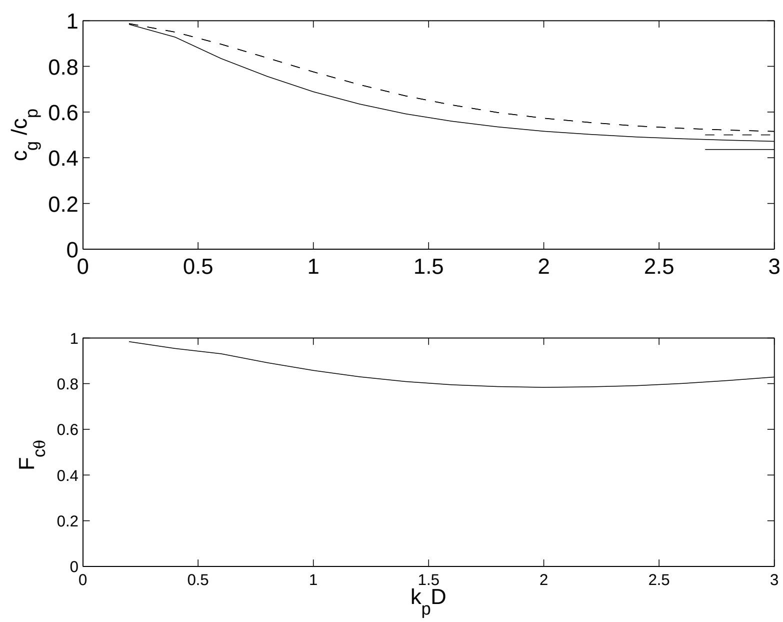

1
0.8
0.6
0.4
0.2
0
c_g/c_p
0
0.5
1
1.5
2
2.5
3
1
0.8
0.6
0.4
0.2
0
$F_{c\theta}$
0
0.5
1
1.5
2
2.5
3
k_pD

Fig. 2a

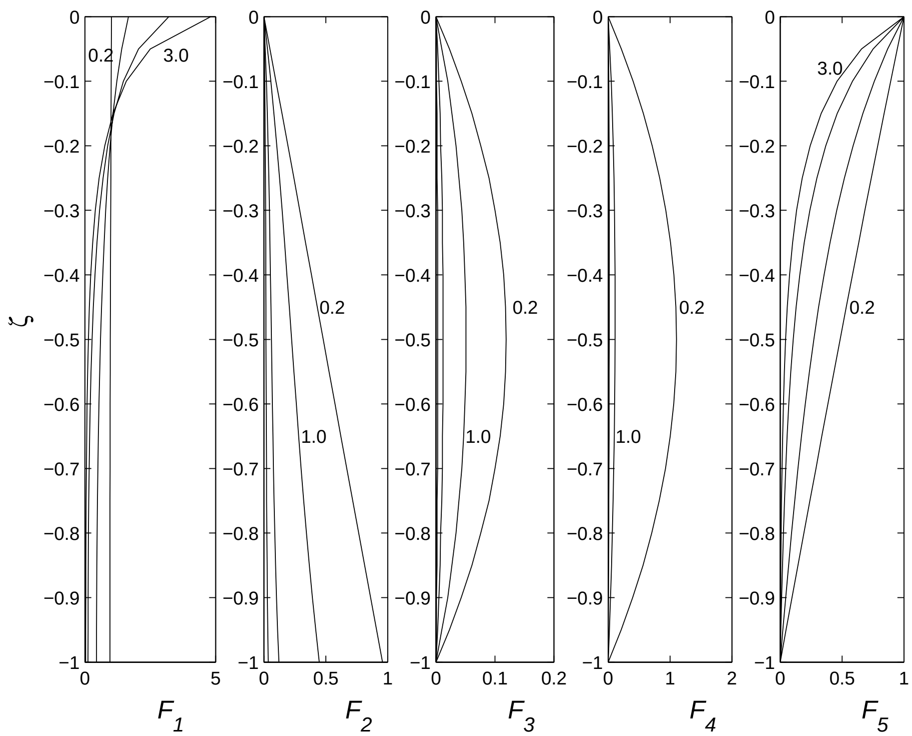

ζ
0.2
3.0
1.0
F_1
F_2
F_3
F_4
F_5

Fig. 2b

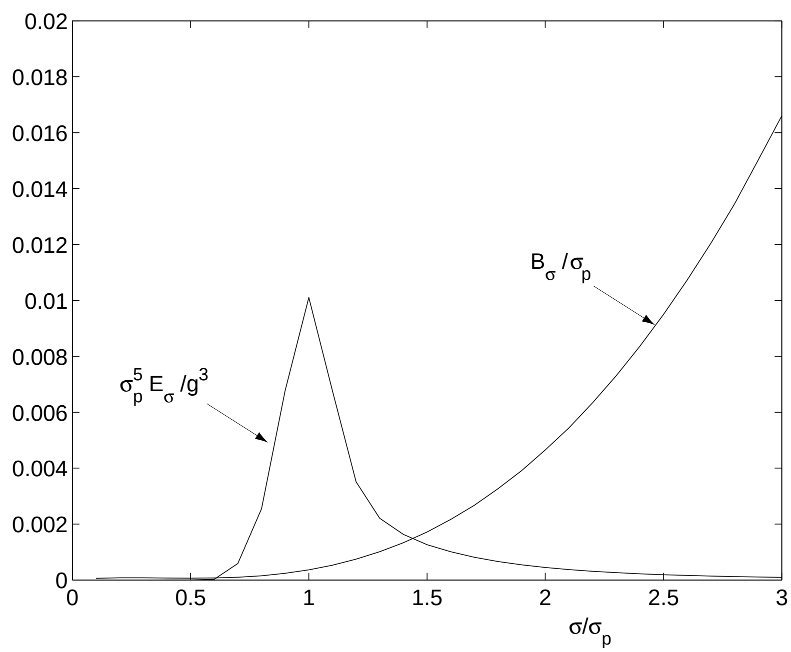

B_σ/σ_p
$\sigma_p^5 E_\sigma/g^3$
σ/σ_p

Fig. 3

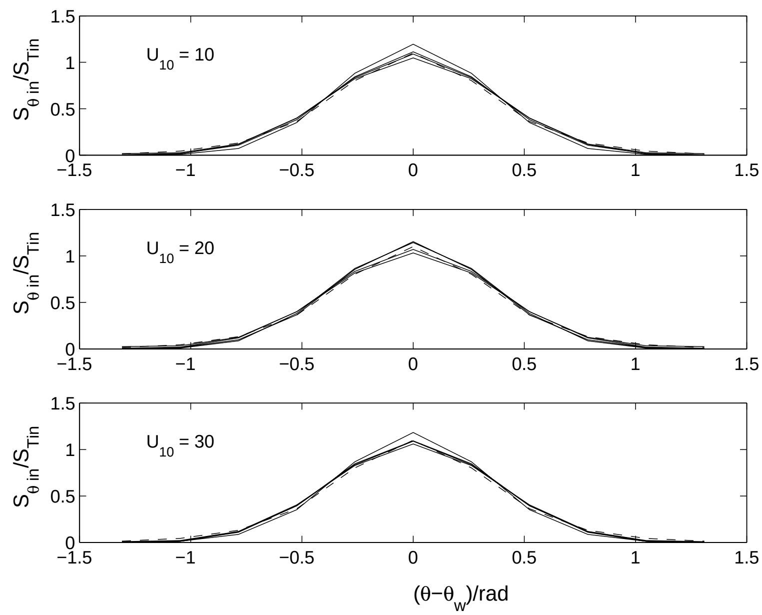
U10 = 10
U10 = 20
U10 = 30
Sθ in/STin
(θ−θw)/rad

Fig. 4

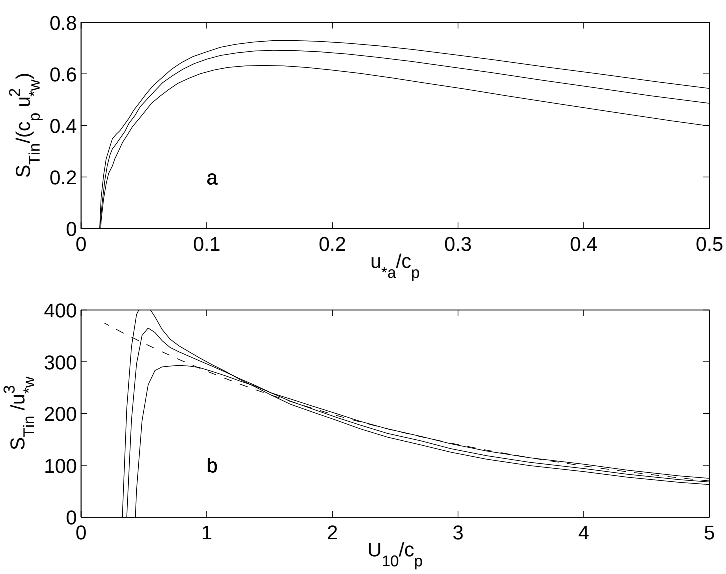
a
STin/(cp u2*w)
u*a/cp
b
STin/u3*w
U10/cp

Fig. 5

.

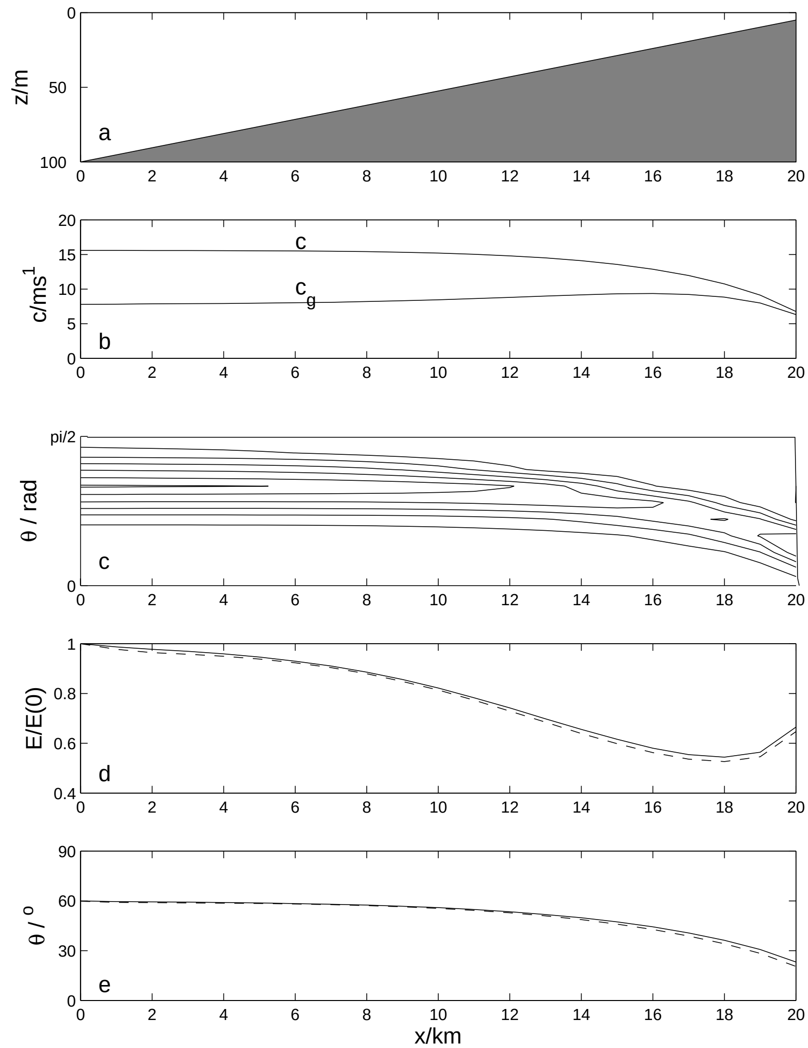

Fig. 6.

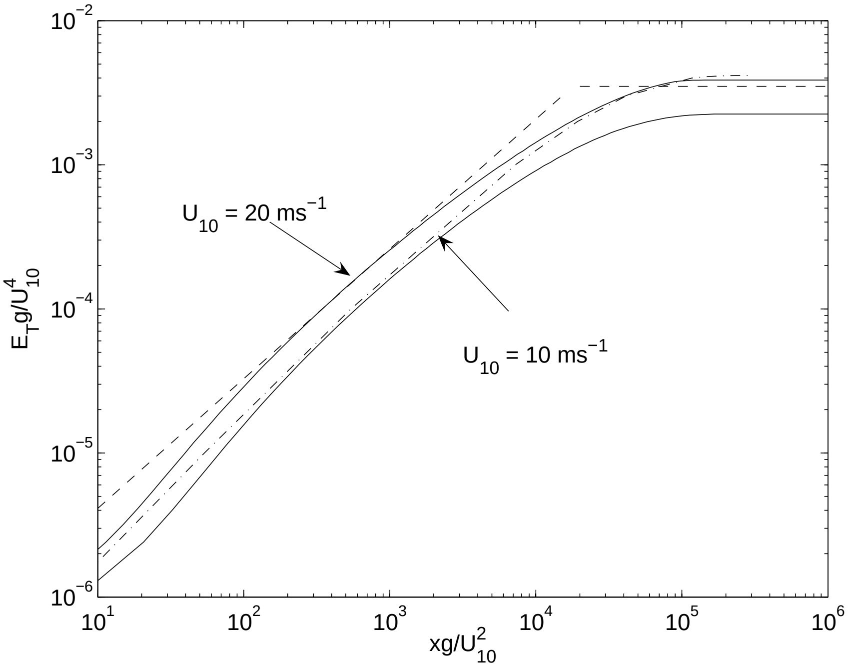

10^{-2}
10^{-3}
10^{-4}
10^{-5}
10^{-6}
$E_T g/U_{10}^4$
U_{10} = 20 ms^{-1}
U_{10} = 10 ms^{-1}
10^1 10^2 10^3 10^4 10^5 10^6
xg/U_{10}^2

Fig. 7

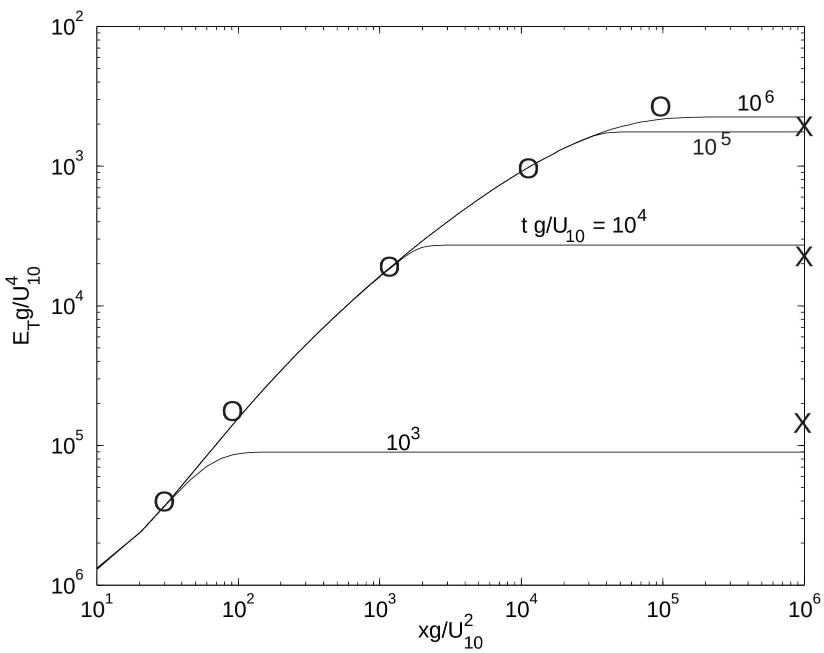

10^2
10^3
10^4
10^5
10^6
$E_T g/U_{10}^4$
10^6
10^5
t $g/U_{10} = 10^4$
10^3
10^1 10^2 10^3 10^4 10^5 10^6
xg/U_{10}^2

Fig.8

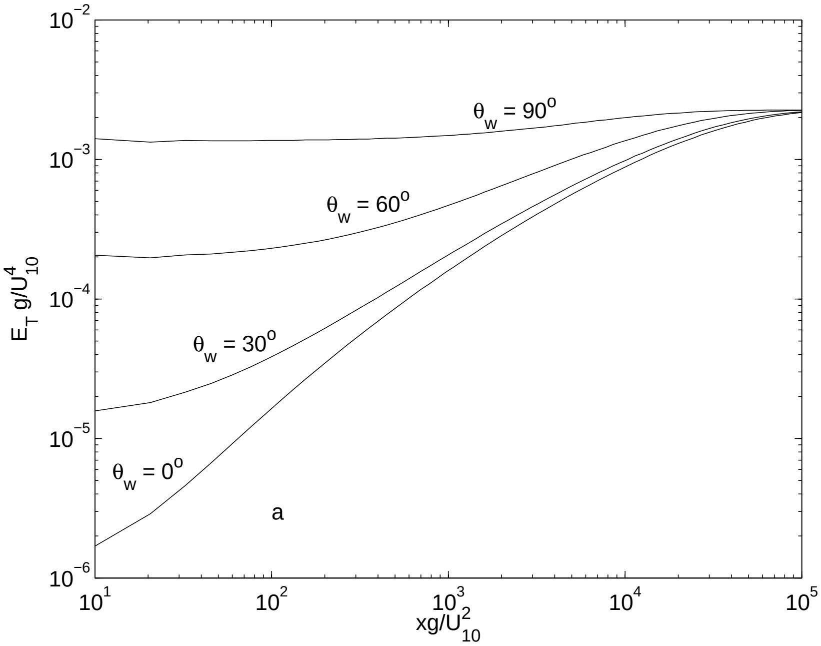

10^{-2}
10^{-3}
10^{-4}
10^{-5}
10^{-6}
$E_T\, g/U_{10}^4$
$\theta_w = 90^o$
$\theta_w = 60^o$
$\theta_w = 30^o$
$\theta_w = 0^o$
a
10^1
10^2
10^3
10^4
10^5
xg/U_{10}^2

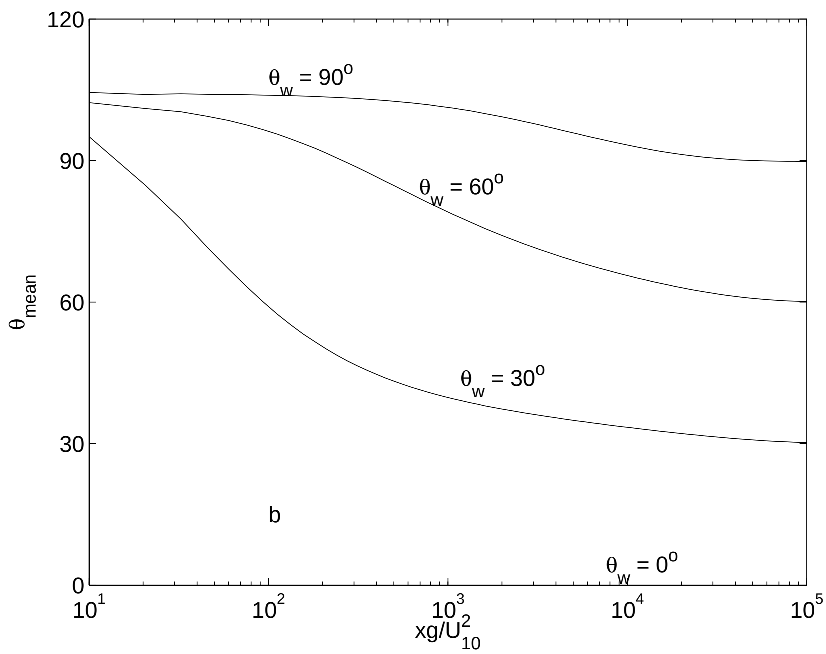

120
90
60
30
0
θ_{mean}
$\theta_w = 90^o$
$\theta_w = 60^o$
$\theta_w = 30^o$
b
$\theta_w = 0^o$
10^1
10^2
10^3
10^4
10^5
xg/U_{10}^2

Fig. 9

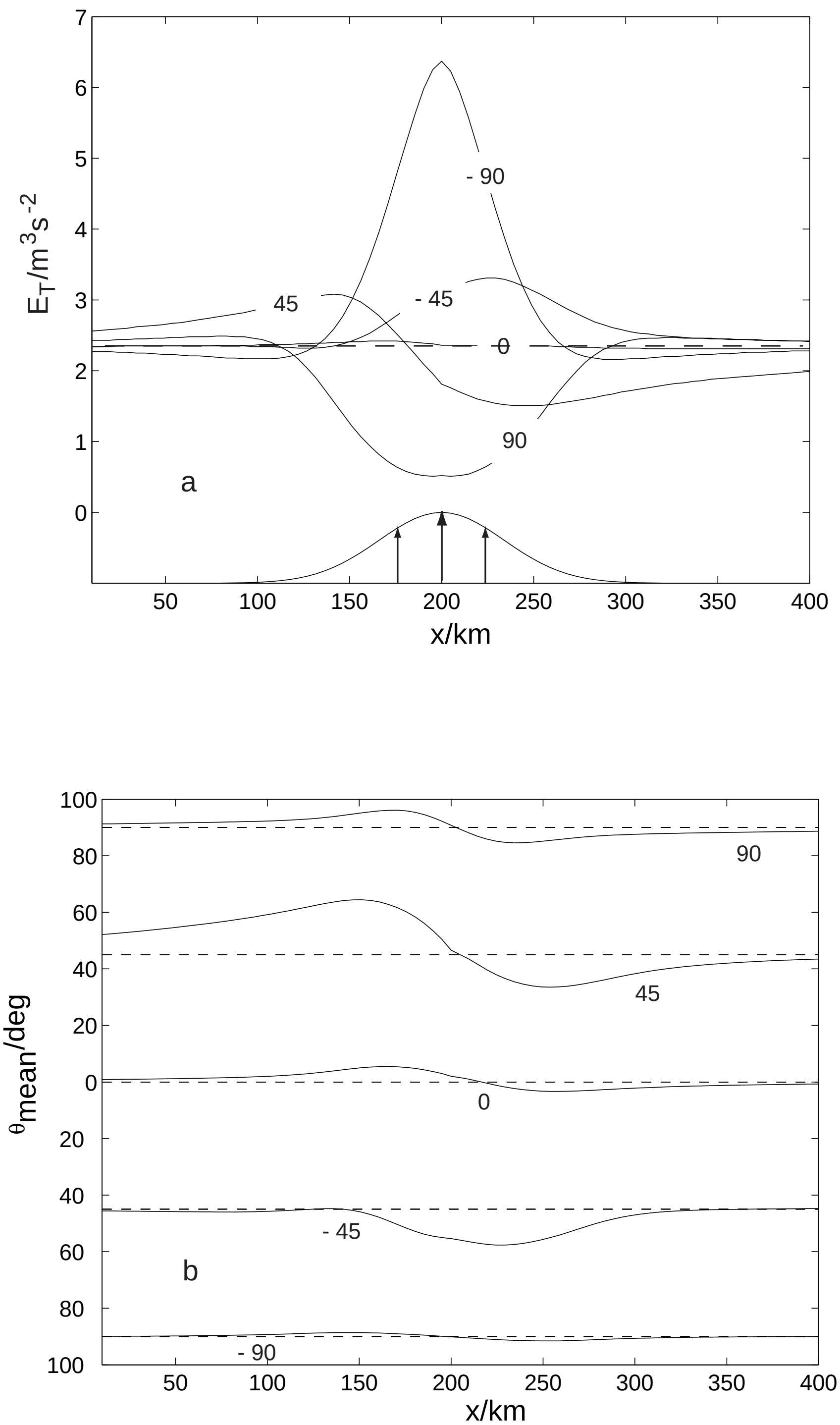

Fig. 10.

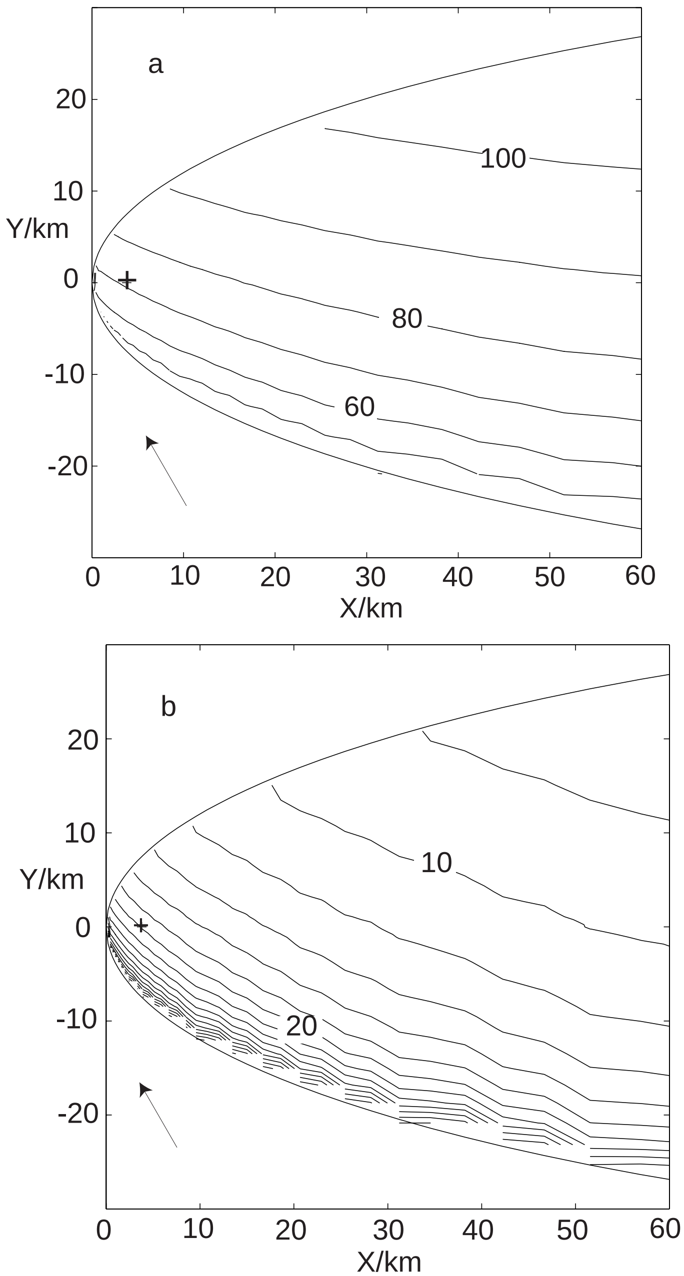

Fig 11

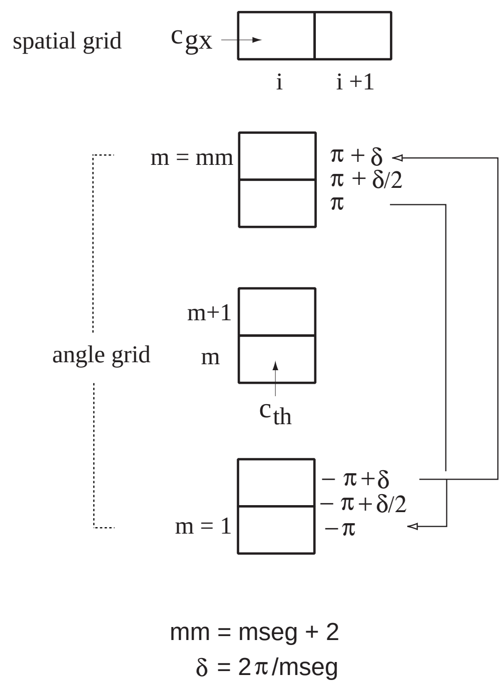
spatial grid
cgx
i
i +1
m = mm
π + δ
π + δ/2
π
angle grid
m+1
m
cth
m = 1
− π + δ
− π + δ/2
−π
mm = mseg + 2
δ = 2π/mseg

Fig.12

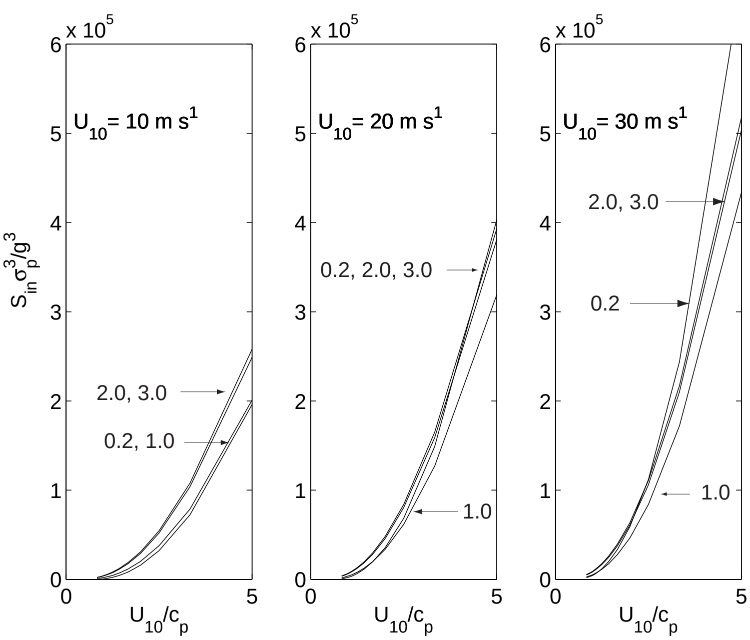
x 10^5
U10= 10 m s-1
U10= 20 m s-1
U10= 30 m s-1
Sinσp^3/g^3
2.0, 3.0
0.2, 1.0
0.2, 2.0, 3.0
1.0
0.2
U10/cp

Fig. 13